Observations of the Storfjorden overflow

Ilker Fer [a], Ragnheid Skogseth [a, b], Peter M. Haugan [a, c] and Pierre Jaccard [a]

[a] Geophysical Institute, University of Bergen, Allégaten 70, N-5007, Bergen, Norway
[b] The University Centre on Svalbard, P.O. Box 156, N-9170, Longyearbyen, Norway
[c] Bjerknes Centre for Climate Research, Allégaten 55, N-5007, Bergen, Norway

Received 13 August 2002; revised 26 February 2003; accepted 27 June 2003

Abstract

The mixing and spreading of the Storfjorden overflow were investigated with density and horizontal velocity profiles collected at closely spaced stations. The dense bottom water generated by strong winter cooling, enhanced ice formation and the consequent brine rejection drains into and fills the depression of the fjord and upon reaching a 120-m deep sill, descends like a gravity current following the bathymetry towards the shelf edge. The observations covered an approximate 37-km path of the plume starting from about 68 km downstream of the sill. The plume is identified as two layers: a dense layer 1 with relatively uniform vertical structure underlying a thicker layer 2 with larger vertical density gradients. Layer 1, probably remnants from earlier overflows, almost maintains its temperature–salinity characteristics and spreads to a width of about 6 km over its path, comparable to spread resulting from Ekman veering. Layer 2, on the other hand, is a mixing layer and widens to about 16 km. The overflow, in its core, is observed to have salinities greater than 34.9, temperatures close to the freezing point, and light transmissivity typically 5% less than that of the ambient waters. The overall properties of the observed part of the plume suggest dynamical stability with weak entrainment. However local mixing is observed through profiles of the gradient Richardson number, the non-dimensional ratio of density gradient over velocity gradient, which show portions with supercritical values in the vicinity of the plume–ambient water interface. The net volume transport associated with the overflow is estimated to be 0.06 Sv (Sv≡10^6 m^3 s^{-1}) out of a section closest to the sill and almost double that as it leaves the section furthest downstream. The weak entrainment is estimated to account for the doubling of the volume transport between the two sections. A simple model proposed by Killworth (J. Geophys. Res. 106 (2001) 22267), giving the path of the overflow from a constant rate of vertical descent along the slope, compares well with our observations.

Author Keywords: Overflow; Cascading; Mixing processes; Marginal seas; Svalbard Archipelago; Storfjorden

1. Introduction

The deep and intermediate Arctic waters are produced mainly on the Arctic shelves where intense and sustained winter cooling leads to formation of dense bottom waters. The heat loss from surface waters of a shelf basin to the atmosphere triggers convection and ice formation. The consequent brine rejection produces brine-enriched shelf water (BSW), particularly in ice-free regions. The BSW accumulates in the basin, which might be enclosed by a sill, and eventually spills over the sill or finds paths down submarine canyons to the deep sea. Upon reaching the shelf edge, the plume of BSW cascades, i.e., descends the continental slope under the combined effects of pressure gradient, frictional forces including the entrainment stress, and the Coriolis force ([Griffiths (1986)]; [Price and Baringer (1994)]). In the course of its descent into the deep ocean, the BSW entrains a substantial volume of water with temperature and salinity of the overlying waters ([Price and Baringer (1994)]). The entrainment, therefore, alters the characteristics of the plume which results in ‘product waters’ that finally settle into the deep ocean. [Killworth (1983)] has reviewed the processes involved in shelf and open-ocean convection. [Price and Baringer (1994)] provide a thorough discussion of overflows and deep-water production by marginal seas. Furthermore, [Baines and Condie (1998)] review the existing observations and modeling of similar downslope flows around Antarctica, together with the dynamical mechanisms by which the flow is achieved.

The ventilation of the deep Arctic Ocean is thought to be achieved mainly by this cascade of cold BSW and studies reveal that the shelf regions contribute significantly to the overall heat and salt balance of the deep Arctic Ocean basins ([Rudels (1986)]). [Rudels and Quadfasel (1991)] have estimated a contribution of about 0.5 Sv (Sv≡10^6 m^3 s^{-1}) from shelf convection into the Arctic deep water, comparable to that through open-ocean convection in the Greenland Sea ([Smethie et al (1986)]). The Barents Sea, where BSW forms underneath coastal polynyas such as the Storfjorden polynya, is a crucial gateway for the main flow into the Arctic Ocean ([Midttun (1985)]). Storfjorden is estimated to supply about 5–10% of

the newly formed waters of the Arctic Ocean ([Quadfasel et al (1988)]). Previous recent studies in the area have dealt primarily with field observations ([Quadfasel et al (1988)]; [Schauer (1995)]; [Schauer and Fahrbach (1999)]) and numerical simulations ([Backhaus et al (1994)]; [Jungclaus et al (1995)]) of the Storfjorden overflow, as well as the variability of ice production and brine formation using satellite remote sensing data ([Haarpaintner et al (2001a) and Haarpaintner et al (2001b)]). Earlier estimates of volume transport of the overflow (Section 5.3) were from single-point moored current meters and assumed constant width and thickness of the overflow, or were from numerical simulations. Mixing of the plume was generally inferred from changes in temperature–salinity characteristics.

In order to investigate the path and the volume transport associated with the Storfjorden overflow and its modification along the path, we conducted a survey of the overflow at closely spaced stations. In particular, our aim was to collect data that could shed light on local mixing mechanisms responsible for the changes en route from the sill of the basin towards the shelf break. The field data set collected for 5 days from 28 May 2001 consists of conductivity, temperature, depth (CTD) and light transmissivity profiles, velocity profiles obtained from a ship-mounted acoustic Doppler current profiler (ADCP), and a Nortek lowered acoustic Doppler current profiler (LADCP) installed below the CTD instrument. The LADCP data are the first of their kind within the Storfjorden overflow and allow for transport estimates using full-depth velocity profiles at each station, albeit hindered by absence of information about temporal variability of the overflow. Recently [Gordon et al (2001)] have reported a similar LADCP survey of the Weddell Sea deep and bottom water. In Section 2 we describe the site and the sampling of the field experiment. Information on tides over the period of the deployment and inter-comparison of ship-mounted ADCP and LADCP records are given in Section 3 together with a description of the variability and the errors associated with the LADCP data. Observations are summarized in Section 4 and subsequently discussed in Section 5.

2. Site and measurements

Storfjorden is an inlet of the western Barents Sea, located in the southeast of Spitsbergen in the Svalbard Archipelago (Fig. 1). The fjord is approximately 190 km long and 190 m deep at its maximum depth. Inner Storfjorden covers an area of about 13 000 km^2 with an approximate volume of 8.5×10^{11} m^3 ([Skogseth et al (2003)]). It is enclosed by the islands Spitsbergen, Barentsøya, and Edgeøya and limited by a shallow bank, Storfjordbanken, in the southeast and a 120-m deep sill at about 77°N in the south.

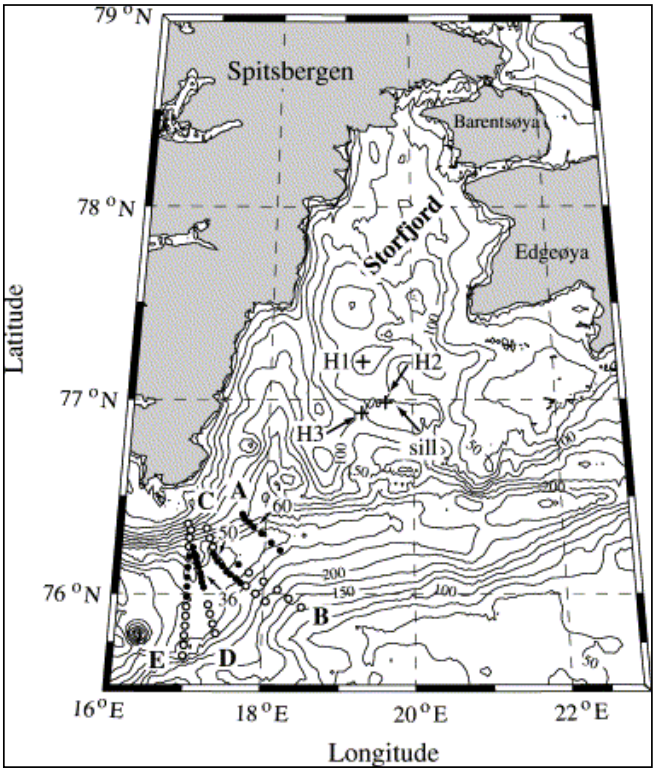

Fig. 1. Bathymetry of the area and locations of the stations occupied by R.V. *Lance* (circles, CTD; dots, CTD and LADCP) along the transects A–E, and the helicopter cruises (+). Stations H1, H2 and H3 of Fig. 5, and stations 36, 50, and 60 of Fig. 6 are indicated. Depth contours are drawn at 25-m intervals. Location of the sill is identified by an arrow.

Observations were made of the overflow of the BSW plume from Storfjorden at densely spaced hydrographic stations occupied by the Research Vessel *Lance*, during 28 May–2 June 2001. A Seabird Electronics SBE911*plus* CTD instrument was equipped with a 1.5 MHz Nortek LADCP and was lowered at a rate of 0.5 m s^{-1}. The LADCP was mounted below the CTD, pointing downward, and recorded 1-s averaged profiles with 0.5-m thick cells within a vertical range of 15–20 m. The sensor accuracies of the

CTD instrument provided by the manufacturer are 1 dbar, 1×10^{-3}°C, and 3×10^{-4} S m^{-1} for pressure, temperature and conductivity, respectively. The light transmissometer, Alphatracka MkII Chelsea Instruments, is accurate to better than 0.3% of the full-scale range. The velocity sampled by the LADCP is accurate to ±1% of the measured velocity. Because of heavy ice inside the fjord, measurements were made only from about 68 km downstream of the sill (Fig. 1). We rely on several hydrographic stations occupied inside the fjord during helicopter cruises carried out on 6 and 23 April 2001 to provide information on the source conditions. SeaBird SBE 19 SEACAT profilers were used during the helicopter cruises with pressure, temperature and conductivity sensors accurate to 0.1% of full-scale range, 5×10^{-3}° C and 5×10^{-4} S m^{-1}, respectively. A total of 10 (helicopter) and 105 (ship) salinity samples were recovered and were used for calibration. During the *Lance* cruise, a ship-mounted RD Instruments Broadband 150 kHz ADCP ran continuously to provide inter-comparison with the LADCP measurements as well as velocity profiles when the LADCP was not run. Navigation data were used to correct the LADCP record for ship drift.

During the *Lance* cruise, 63 surface-to-bottom CTD casts were performed. The BSW plume was detected in 33 of the stations where LADCP profiles were made (see Fig. 1). At the LADCP stations, the downcast typically was followed by about 10 min of sampling while the depth of the sonde was maintained constant (±2 m), providing for reliable and sufficient data within the plume. Depending on the thickness of the plume, this constant-depth sampling was repeated at several levels, each with duration of approximately 10 min and 10–15 m above the preceding, until the sonde was out of the plume. A typical time series, in which four levels were sampled for approximately 10 min, is shown in Fig. 2. The LADCP data allow examination of the velocity structure associated with the plume to within 1 m of the bottom with a vertical resolution better than 0.5 m. Whilst the LADCP data provide for a snapshot of the velocity field at each station, they may not be representative of the long-term mean.

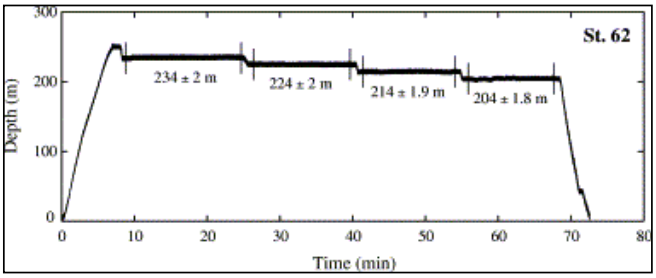

Fig. 2. Time series of the depth (via pressure) record from the profile obtained at station 62 of section A. The mean values and one standard deviation of the depth calculated over each ~10 min portion when the depth was maintained approximately constant are indicated.

Throughout the paper, potential temperature is used, profiles of temperature, salinity, and velocity are averaged into 1-m depth bins, and salinity is given on the practical salinity scale.

3. Tides, ADCP and LADCP

We shall rely on numerical simulation results and data from three Aanderaa current meters deployed at the shelf break at the 300-m isobath (mooring SB1; location marked in Fig. 14, introduced later) for tidal information in the vicinity of the observation site. The mooring data (kindly provided by Ursula Schauer), after filtering of the tidal and inertial signals, were presented in [Schauer and Fahrbach (1999)] but were not analyzed with respect to tides. A database of modeled tides is publicly available (http://www.ims.uaf.edu/tide/index.html) providing for the amplitude and phase of zonal and meridional components of the depth-averaged velocity related to 8 tidal constituents with a spatial resolution of 10′×10′ in the Arctic Ocean and the Nordic Seas (see also [Kowalik and Proshutinsky (1993)]; [Kowalik (1994)]). We have extracted the data within 76°–76°30′N and 17°–18°E for the M_2, K_1, O_1, and S_2 constituents and evaluated the zonal and meridional components of the depth-averaged tides. The time series derived for each component is shown in Fig. 3 and compared to the velocity measured by the LADCP and the ADCP. The data are averaged over the depth range of the ADCP (i.e., within 14–190 m of the water column) both for the LADCP and the ADCP, providing for an inter-comparison and also removing possible effects of the BSW flow adjacent to the bottom boundary, which were not incorporated in the tidal simulations. The start time of each profile and the corresponding station number are also indicated relative to 0 h of the day of the first LADCP station (station 14). The error bars on the ADCP data show one standard deviation over several profiles obtained within the duration, typically 1 h, of the LADCP sampling. The east and the north components of the depth averaged velocity measured by both instruments agree fairly well and follow the tidal oscillations derived from the simulations.

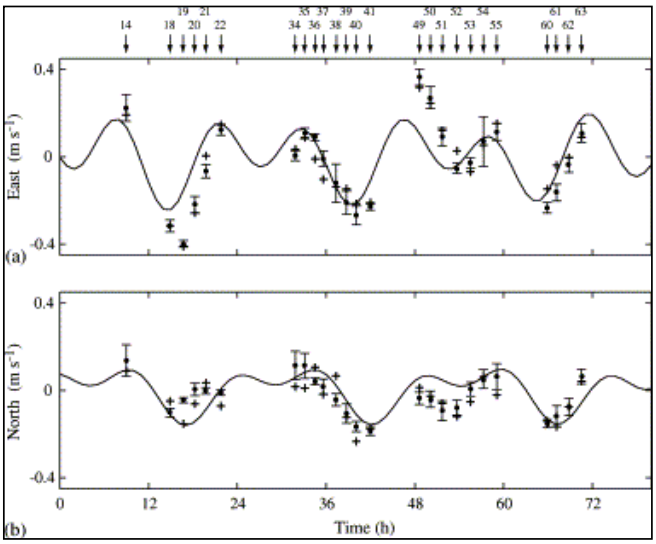

Fig. 3. East (a) and north (b) components of the velocity measured by CTD-mounted LADCP (plus signs), ship-mounted ADCP (dots), and depth averaged tides after Kowalik and Proshutinsky (solid line). Time is measured from 0 h of the day of station 14. Measured LADCP and ADCP components are depth averaged within 14–190 m, hence provide for intercomparison. The error bars are one standard deviation over the total number of profiles obtained by ADCP during LADCP sampling. The arrows at the top show the start time of the stations indicated by the corresponding numbers.

The latitude where the semidiurnal frequency, M_2, equals the inertial frequency, the so-called 'critical latitude', is at 74°28′18″N, approximately 170 km south of our measurement site. At the critical latitude the tidal current is strongly depth-dependent and the sense of rotation of the tidal ellipse may vary with depth. Using one-year-long (1993/94) time series of current data recorded at SB1 location (Fig. 14), the tidal ellipses for the most dominant diurnal and semi-diurnal constituents at 64 (236), 167 (133), and 290 (10) m depth (height above bottom) were derived by tidal harmonic analysis ([Pawlowicz et al (2002)]) and are shown in Fig. 4. The diurnal components have negative eccentricity (clockwise rotation) at all depths, whereas both diurnal components change sign (counter-clockwise rotation) at 10 m off bottom, hence suggesting baroclinic tides. Tides are depth dependent with magnitude decreasing with increasing depth, particularly significant for K_1 and M_2 components. Critical latitude effects on currents near Ronne Ice Shelf in the Weddell Sea have been discussed by [Foldvik et al (2001)]. There the critical latitude was about 220 km north of their mooring site, a relative distance comparable to ours. The depth dependent behavior of the tidal current near the critical latitude in the Barents Sea that we have observed confirms theoretical predictions ([Furevik and Foldvik (1996)]).

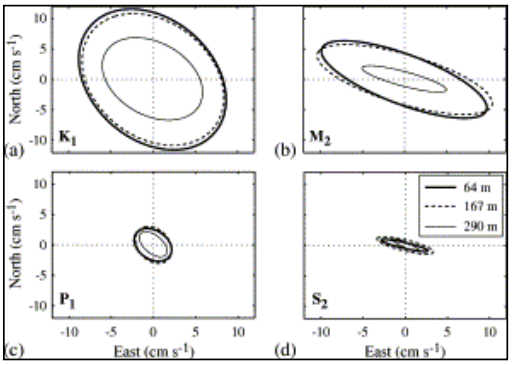

Fig. 4. Tidal ellipses of diurnal (a) K_1, (c) P_1, and semi-diurnal (b) M_2, (d) S_2 constituents derived from the data recorded by current meters at 64, 167, and 290 m depth from SB1 at 300-m isobath (for location see Fig. 14). The deepest current meter was at 10 m above the bottom. The legend given in (d) is identical for all the panels. Values of eccentricity at 64 m are −0.66, −0.35, −0.69, and −0.16 for K_1, M_2, P_1, and S_2, respectively. Those at 167 m are −0.68, −0.35, −0.63, and −0.25. The corresponding values at 10 m above the bottom are −0.70, +0.22, −0.53, and +0.20, with positive values indicating counter-clockwise rotation.

Modeled depth averaged tidal residual currents are negligible with velocities less than 1 cm s^{-1} at our measurement site, in Storfjordrenna, but strong anticyclonic eddy circulation around Bjørnøya and Hopen has been reported (see Fig. 7 of [Gjevik et al (1994)]).

In the following, we attempt to assess the variability and errors in the velocity profiles obtained from the LADCP. The instrument continuously profiled while being lowered, hence several data points were acquired in each 1-m depth bin prior to averaging. A large amount of data was collected within the

portions of the profile where the depth was maintained constant. After calculating standard deviations at each depth-bin of the profile, a profile standard deviation SD_p can be estimated by

$$SD_p = \sqrt{\left(\sum_{i=1}^{n} df_i\, SD_i^2\right) / \left(\sum_{i=1}^{n} df_i\right)}. \quad (1)$$

where n is the total number of 1-m depth bins, and df is the degrees of freedom in each bin. The summation is carried out until the deepest bin has been reached. The standard error for each profile can then be calculated as $SE=SD_p/n^{1/2}$. Calculated values of SE vary within 1–3 cm s^{-1} and mean SE over the 33 LADCP profiles is 2 cm s^{-1}.

Statistics of the recorded velocity within the plume at three representative stations (60, 50 and 36; see Fig. 1 for the location of the profiles) are summarized in Table 1 and Table 2. In Table 1, the mean sampling depth of each constant-depth portion is given together with its duration, the east and north components of the measured velocity and the percentage of the data with signal-to-noise ratio (SN) >1.5. Here, SN is defined as the ratio of the signal strength to the instrumental and background noise estimated by inspecting the signal recorded in the air and low-quality data from the furthermost bins. There are large variations in the velocity data with standard deviations exceeding 0.15 m s^{-1}; however, 70% (on the average) of the data is spanned by ±1 standard deviation, typical of normal distributions. The signal-to-noise ratio is >1.5 for 81% of the data, on the average.

Table 1. Variability of the LADCP data within the plume

Station	Sampling depth (m)	Duration (min)	U, east (m s^{-1})	V, north (m s^{-1})	SN>1.5 (%)
60	265±2.6	14.2	−0.08 ± 0.16	−0.35 ± 0.17	78
	254±2.0	13.2	−0.12 ± 0.18	−0.31 ± 0.18	79
50	296±2.4	12.9	0.13 ± 0.17	0.11 ± 0.17	89
	284±2.3	12.6	0.14 ± 0.17	0.11 ± 0.17	81
	274±2.0	11.0	0.16 ± 0.2	0.17 ± 0.19	82
	264±2.1	11.3	0.23 ± 0.16	0.12 ± 0.18	79
36	295±3.0	8.3	−0.21 ± 0.19	0.10 ± 0.19	85
	278±1.8	7	−0.11 ± 0.16	0.14 ± 0.15	76

First column is the station number. Sampling depth is the depth averaged over the duration given in the third column when the depth was maintained constant. The sign '±' indicates one standard deviation over the duration. Last column is the percentage of the data with signal to noise ratio exceeding 1.5.

Table 2. The ranges of correlation coefficient calculated for east and north components of the velocity recorded by the LADCP at stations 60, 50 and 36

Station	East		North	
	r_{1m}	r_{tb}	r_{1m}	r_{tb}
60	0.16–0.45	(0.11)–0.31	(0.10)–0.30	(0.10)–0.20
50	(0.05)–0.40	(0.05)–0.20	(0.05)–0.40	(0.05)–0.20
36	(0.10)–0.45	(0.10)–0.20	(0.05)–0.35	(0.05)–0.20

Values in brackets are not significantly greater than zero at 95% level of significance. The correlation calculated over each consequent 1-m increment is r_{1m}. The correlation between the topmost and the bottommost bin of each constant-depth sampling portion is r_{tb}.

The data recorded during each constant-depth portion can be re-arranged as time series (of ~7–14 min) of vertically 1-m averaged values. Then the correlation coefficient can be calculated at each consequent 1-m increment (r_{1m}) and between the topmost and the bottommost bin (r_{tb}) for each profile. The range of both correlation coefficients calculated in this fashion is given in Table 2, separately for east and north components of the velocity. Both components of the horizontal velocity are correlated at 1-m intervals with values significantly greater than zero, and this correlation persists over top-to-bottom range of typically 15–20 m in the vertical, notably reducing to about half of that obtained for 1-m increments. Examination of 1-s averaged velocity profiles prior to 1-m bin averaging shows that correlation disappears with increasing distance from the instrument, because of high noise associated with the furthest bins. Correlation ranges given in Table 2 suggest that a sufficient amount of averaging was made and noise was eliminated to a certain extent. Considering the small standard error, high SN, and persistent significant correlation from 1 m to larger vertical separations, we conclude that we can use the LADCP data within the overflow with confidence, even though the standard deviation is large in the constant-depth sampling portions.

4. Observations

4.1. Source conditions

In the interior Storfjorden, i.e. north of the sill, a mean annual cycle can be described following [Anderson et al (1988)] and [Haarpaintner et al (2001a)]. In winter, the entire water column is approximately at freezing point temperature and salinity-stratified. In summer a ~30 m thick surface layer of relatively warm and fresh water (S~34.3) develops due to surface warming and melting of sea ice. A bottom layer with S>35 and with temperatures close to the

freezing point lies underneath an intermediate layer (between ~30 and 100 m depth) of *S*~34.6. Bottom temperatures remain <−1.5°C in the summer. The salinity of the BSW in the fjord has strong interannual variability. [Quadfasel et al (1988)] reported *S*>35.4 in 1986 whereas in summer 1991, it was observed to be 35.02 ([Schauer (1995)]) and was less than that of the Atlantic water (AW) in 1993 ([Schauer and Fahrbach (1999)]). The evolution of the polynya and the consequent brine rejection in the fjord have been described by [Haarpaintner et al (2001a)]. The hydrography, BSW formation and vertical mixing in the interior Storfjorden are topics of an ongoing study, and only some sample profiles obtained prior to the Lance cruise will be shown to describe the source conditions for the observed overflow.

Profiles of temperature, salinity and density derived for the selected stations inside the fjord and in the proximity of the sill are shown in Fig. 5. Inside the fjord the profiles reveal that the temperature of the entire water column is close to the freezing point, notably 0.1–0.2°C warmer within 30–80 and 110–140 m depth, and below about 75 m depth salinity increases gradually with depth exceeding 35.5 at the deepest point (Fig. 5a). However, in the vicinity of the sill the salinity is around 35.1 (Fig. 5b–c). The water column is predominantly salinity stratified, and several profiles show statically unstable layers which may lead to overturns.

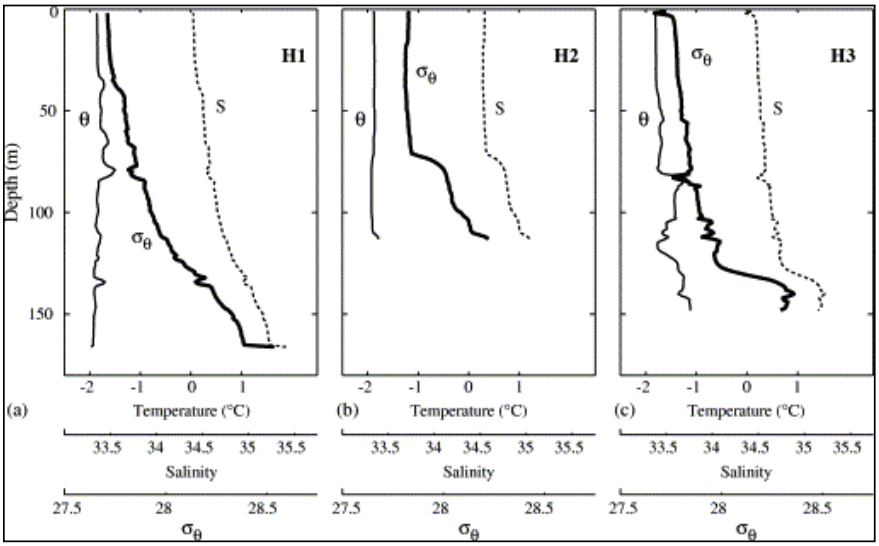

Fig. 5. Potential temperature, θ (solid line), salinity, *S* (dotted line), and $\sigma\theta$ (thick line) profiles derived from on-ice measurements at stations H1 (a), H2 (b), and H3 (c) of the helicopter cruise in April 23, 2001. The locations of the stations are shown in Fig. 1.

4.2. Downstream development

Topography plays a major role in spreading of dense water masses. The BSW that filled the depressions of the fjord flows downslope following the bathymetry once it has reached the level of the sill. Downstream development of the plume is depicted in Fig. 6 for stations 60, 50, and 36 of sections A, C, and D, respectively. A preliminary inspection of the profiles suggested that the portions of the plume adjacent to the bottom were relatively homogenous in the vertical with small density gradients (layer 1), whereas a relatively thick mixing layer with large vertical density gradients (layer 2) was present between layer 1 and the ambient water. Therefore, in our analysis of the plume we define layer 1 (with $\sigma\theta$>28.1, and typically $d\rho/dz<3\times10^{-3}$ kg m^{-4}) underlying layer 2 ($27.95<\sigma\theta\leqslant28.1$, and typically $d\rho/dz\geqslant3\times10^{-3}$ kg m^{-4}). Several exceptional profiles, e.g. station 36 (Fig. 6g), had larger density gradients in layer 1; however, we assume that they have negligible effect on the following analysis concerning layer 1. All salinity profiles presented in Fig. 6 show a salinity minimum which strengthens the density gradient in the upper part of the plume. This might be partly responsible for the observed two layer structure further downstream which would also be supported by limited vertical extent of turbulent mixing generated by bottom irregularities. The structure of both layers is completely spanned by the array of sections C, D, and E, each having at least one station at both ends with no plume water present. At section A, the onshore depth of the plume is estimated as the depth where the 27.95 isopycnal at station 63 intersects the bottom when followed horizontally towards the shore. Using the known station locations and the measured properties we can estimate the height and the width of the plume as well as the mean temperature, salinity, and $\sigma\theta$ for each section. Calculated values for sections A, C, D, and E are summarized in Table 3 for both layers.

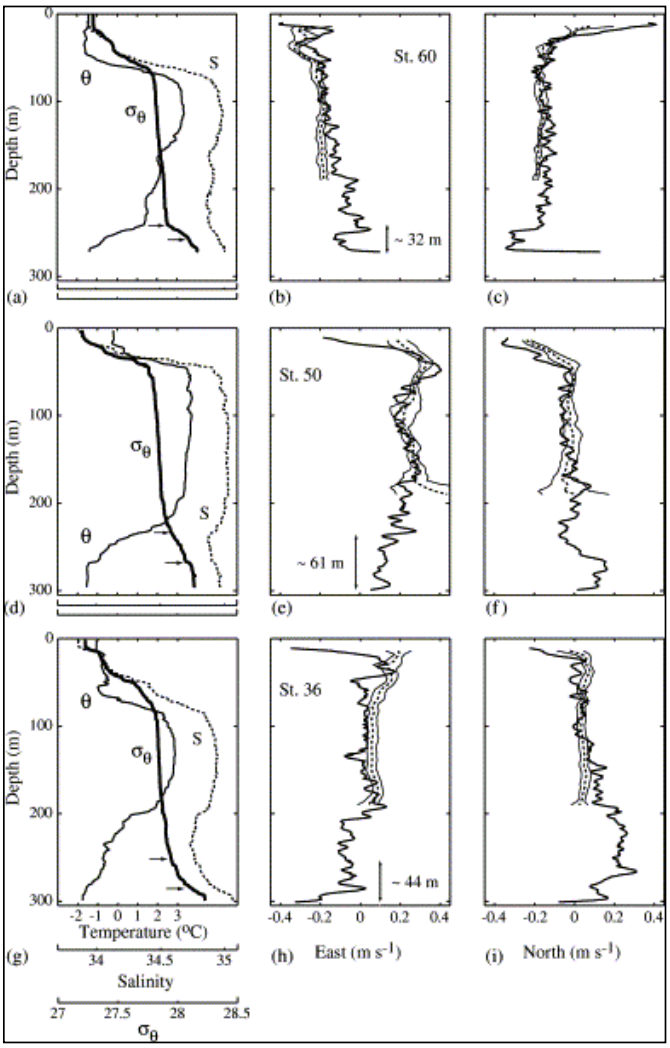

Fig. 6. Downstream development of the plume shown for stations 60 (a–c), 50 (d–f), and 36 (g–i) of sections A, C, and D, respectively. In (a), (d), and (g) temperature, θ (solid line), salinity S (dotted line), and $\sigma\theta$ (thick line) profiles are shown. Profiles of the east component of the velocity measured by the LADCP (thick line) and the ADCP (dashed line) are given in (b), (e), and (h). The corresponding profiles for the north component are given in (c), (f), and (i). The envelopes around the ADCP profiles show one standard deviation derived over the number of profiles obtained during the LADCP sampling. The LADCP profiles derived using 1-m vertically averaged values are smoothed running a 5-data windowed moving average. The arrows in (a), (d), and (g) mark the depth of layers 1 (deepest) and 2. The approximate height of the plume is indicated in (b), (e), and (h), for each station.

Table 3. Mean properties of the plume derived for sections A, C, D and E

	Section A		Section C		Section D		Section E	
	Layer 1	Layer 2	Layer 1	Layer 2	Layer 1	Layer 2	Layer 1	Layer 2
Width (km)	10	22	22	36	22	42	16	38
Height (m)	17±2	22±10	27.5±3	40±15	14±9	31.5±19	8.5±1	20±11
S	34.97±0.02	34.90±0.03	34.97±0.03	34.87±0.02	35.0±0.04	34.87±0.02	35.01±0.02	34.89±0.03
θ (°C)	−1.4±0.3	−0.3±0.5	−1.6±0.09	−0.45±0.3	−1.4±0.4	−0.47±0.5	−1.5±0.3	0.1±0.4
σ_θ	28.14±0.02	28.03±0.02	28.14±0.03	28.02±0.01	28.16±0.04	28.01±0.01	28.17±0.02	28.01±0.03

The values are averaged over each section for each layer and '±' denotes one standard deviation.

At the beginning of the overflow, the plume mixes with relatively fresh East Spitsbergen Water (ESW). Because of the ice mentioned before this part was not resolved in our survey. Further downstream, the upper 200 m of the water column at Storfjordrenna is composed of warm and saline AW (see Fig. 7, Fig. 8 and Fig. 9), which has approximate salinity of the modified plume water after being mixed with the ESW. Here, the plume appears as a cold intrusion into the equally saline AW. The cold (θ<0°C) and fresh (S<34.5) Arctic Water advected from the north-east and the AW entering between the Bjørnøya and Svalbard are separated, at the surface, by the Polar Front which typically follows the 150-m isobath in the summer ([Loeng (1991)]). Along all sections two cores of warm and saline AW are present which can be identified as a northern and a southern core lying between 75 and 200 m depth, suggesting a cyclonic circulation along the Polar Front. A similar circulation pattern has been reported before (e.g., see Fig. 4 of [Schauer (1995)]). At sections D and E (Fig. 8 and Fig. 9) the cores comprise θ=3.5°C and S=35 contours whereas around section A (Fig. 7) both cores are slightly colder and fresher, probably because of the proximity of the Polar Front and the associated mixing with colder and fresher Arctic Water.

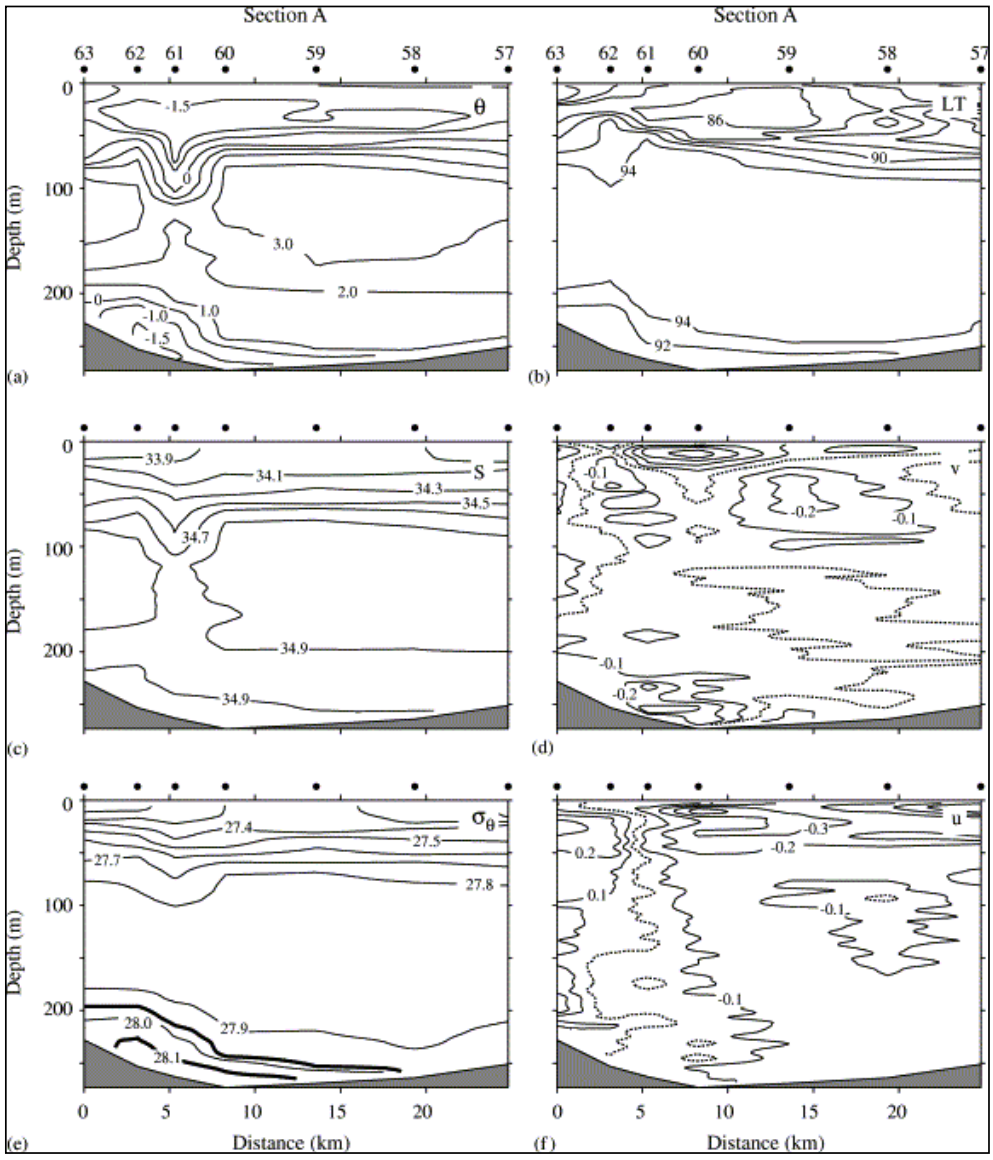

Fig. 7. Contours of (a) potential temperature, θ, (b) light transmissivity, LT, (c) salinity, *S*, (d) north component, *v*, of the velocity recorded by the LADCP, (e) $\sigma\theta$, and (f) east component, *u*, of the velocity recorded by the LADCP derived for section A (see Fig. 1) from profiles taken at the stations indicated by dots over each panel. The profiles are 1-m depth averaged and then smoothed over 5-data points (velocity profiles are first converted to east and north components). Contours are drawn at 1°C intervals for θ (−1.5°C isotherm is also included), 0.2 for S, 0.1 for $\sigma\theta$, 2% for LT, and 0.1 m s^{-1} for *u* and *v*. Dotted contour in (d) and (e) is $u=v=0$. The 28.1 and 27.95 isopycnals identified by firm lines in (e) mark layers 1 and 2, respectively, with the latter showing the approximate cross-sectional extent of the plume.

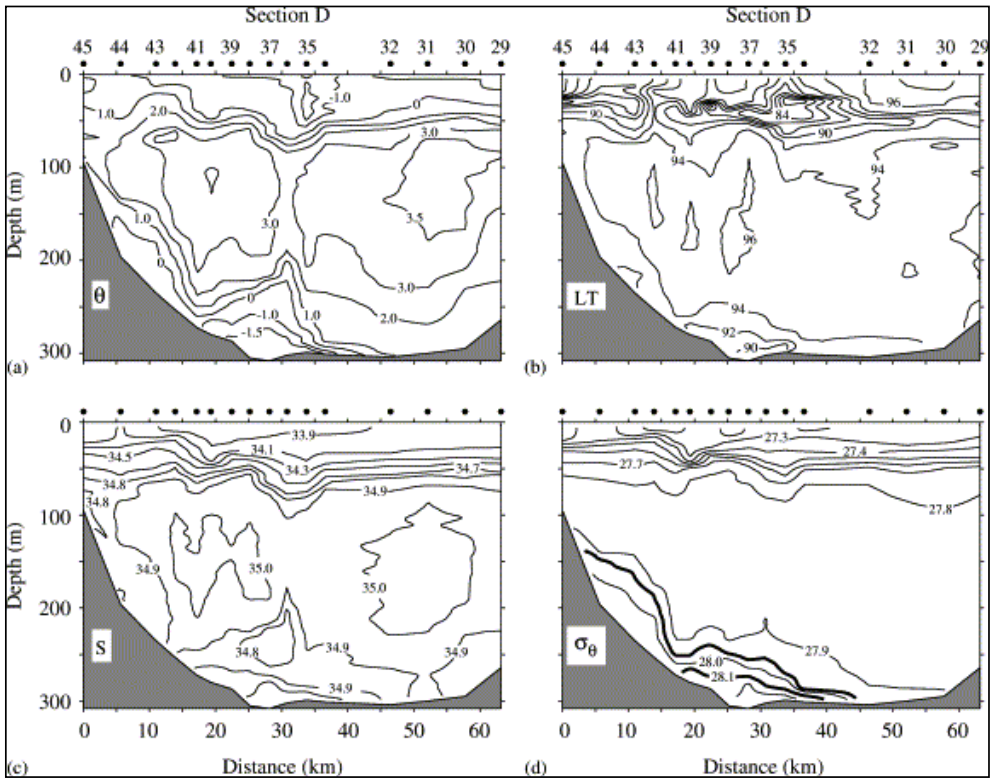

Fig. 8. Contours of (a) potential temperature, θ, (b) light transmissivity, LT, (c) salinity, *S*, and (d) $\sigma\theta$, derived for section D (see Fig. 1) from profiles taken at the stations indicated by dots over each panel. The profiles are 1-m depth averaged and then smoothed over 5-data points. Contours are drawn at 1° C intervals for θ (–1.5°C and 3.5°C isotherms are also included), 0.2 for *S* (34.8 and 35.0 contours are also included), 0.1 for $\sigma\theta$, and 2% for LT. The 28.1 and 27.95 isopycnals identified by firm lines in (d) mark layers 1 and 2, respectively, with the latter showing the approximate cross-sectional extent of the plume.

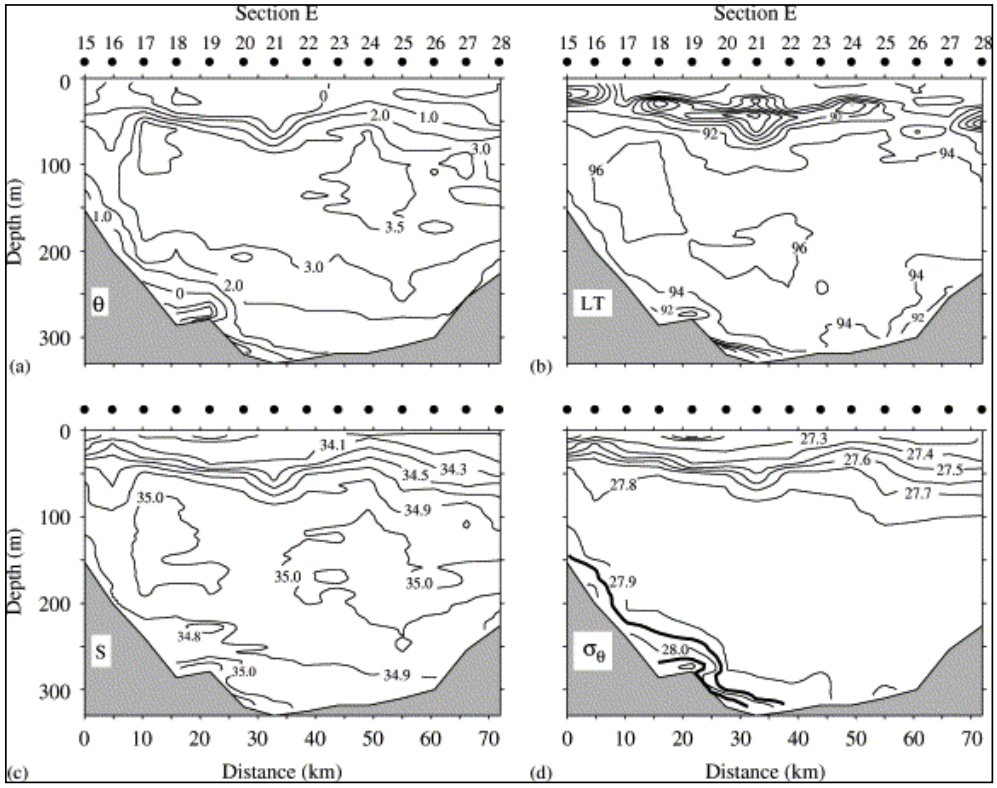

Fig. 9. Same as Fig. 8, but for section E.

The cold, θ<0°C, and saline, *S*>34.9, plume of BSW is apparent adjacent to the sloping bottom close to the shore (Fig. 7, Fig. 8 and Fig. 9). The plume observed at section A is associated with distinct negative values of north component of the velocity exceeding 20 cm s^{-1} (Fig. 7d). The light transmissivity within the plume is about 5% less than that of the ambient water in all sections suggesting an enhanced suspended sediment concentration due to relatively higher velocity of the plume. At sections D and E there is a patch of water above the BSW marked with the 34.8 isohaline. Both sections suggest that there may be a contribution from shelf waters of the onshore region which finds an equivalent depth within or above layer 2, but beneath the AW. This will be discussed later in Section 5.

The downstream development of the onshore and offshore depth and the section averaged height and width of the plume are shown in Fig. 10. The depths of

the onshore and offshore edge of the overflow and the plume width are identified by the 27.95 isopycnal and shown separately. The height is defined as the sum of the thicknesses of layers 1 and 2. The height and width shown in Fig. 10 comprise the whole plume and corresponding properties of the individual layers 1 and 2 are given in Table 3. The total cross-sectional area associated with layer 1 decreases by 20% on its path from section A to E, increasing its width while suppressing its height. Layer 2, however, increases its cross-sectional area by approximately 60% (Table 3). [Jungclaus et al (1995)] predict a width of 23 km for the 40-m height contours for the overflow which is comparable to 22 km width for the observed 39-m height at section A. The onshore and offshore edges of the plume have flowed down the slope to about 140 and 320 m depth, respectively, at section E (Fig. 10a).

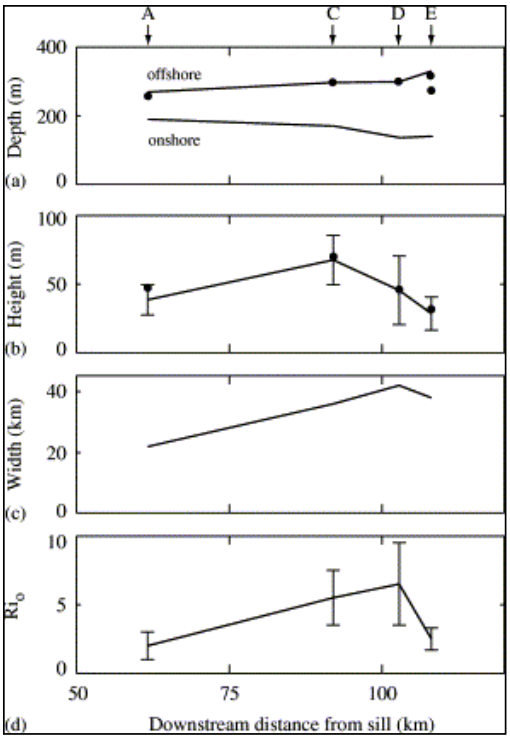

Fig. 10. Downstream development of (a) depth, the section averaged (b) height, (c) width, and (d) the overall Richardson number, Ri_o, associated with the Storfjorden overflow. The sections are indicated by arrows at the top. Onshore and offshore depth of the plume are shown separately in (a). The dots in (a) and (b) mark the property of the core of the plume at each section. For section E, the depth of station 20 is also included in (a). The error bars in (b) and (d) show 1 standard deviation over calculated values of each section. Horizontal axis is the downstream distance calculated from the sill following the path of the overflow. Ri_o is calculated between layer 2 and the ambient waters using the relative velocity of layer 2 with respect to the ambient water.

The LADCP-derived velocity profiles were converted into along and across-section components (Fig. 11). In both sections the LADCP data show relatively large speed out of the section within the plume. The square of the shear over 10-m vertical separations between 50-m depth and the bottom were calculated and compared for LADCP and geostrophy (Fig. 11c–f). Salient features near the vicinity of the plume agree fairly well, e.g. two cores of enhanced shear in both sections. We note that the quality of the LADCP data is better within the plume where constant-depth sampling was made and more data were used in averaging.

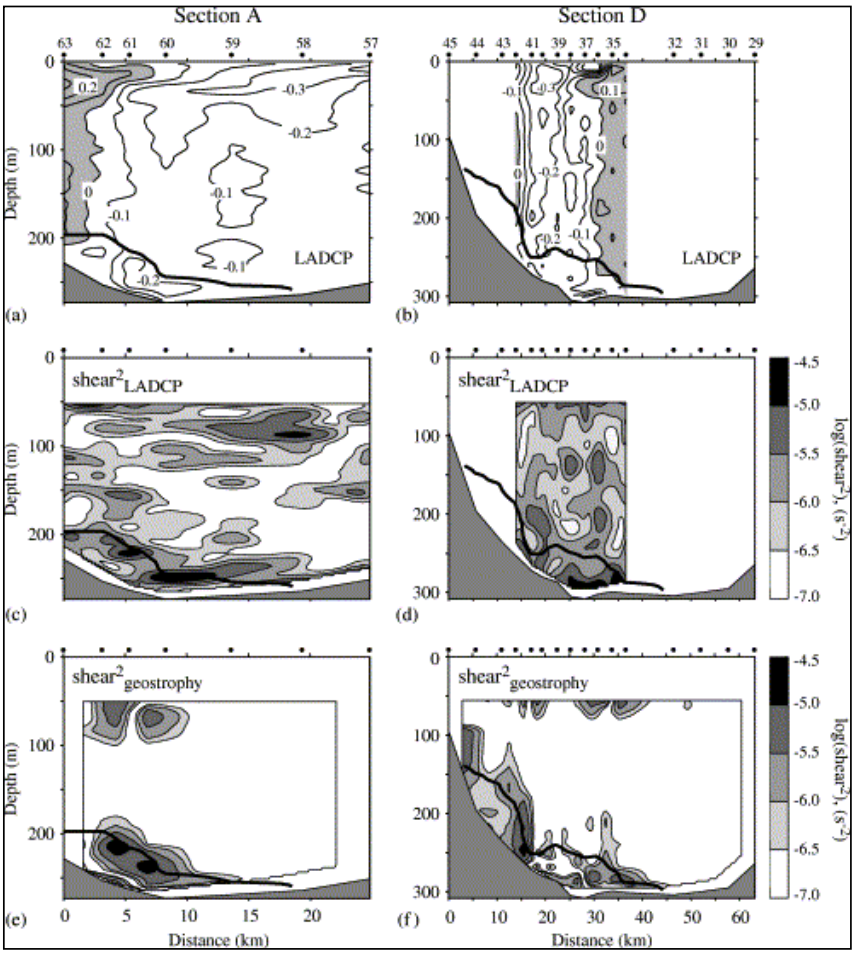

Fig. 11. The contours of the across-section component of the velocity recorded by the LADCP (negative values indicate flow out of the section in downstream direction) derived for (a) section A and (b) section D. The LADCP record is 1-m depth averaged and then smoothed over 5-data points. The portions of the water column moving into the page, i.e. toward the sill, are shaded. Panels (c) and (d) show contours of log(shear^2) between 50 m and bottom derived from the LADCP record. Panels (e) and (f) show those obtained from geostrophic velocity calculated from CTD profiles. A vertical separation of 10 m was used in shear calculations. In all panels the thick line is the height of the plume estimated as the sum of layers 1 and 2 thicknesses.

The velocity of the plume relative to that of the ambient water, estimated as the mean velocity over approximately twice the height of the plume above layer 2, is shown in Fig. 12, together with isotherms derived from the bottom temperatures. The southward flow through section A, followed by spreading and westward flow through sections D and E are notable and the plume, here identified with isotherms <0°C, follows the bathymetry. However, the velocity structure in the plain Storfjordrenna (section C) is not uni-directional but has a pattern suggesting an anticyclonic eddy at the bottom. Due to the depth dependency (Fig. 4) and particularly the change in sense of rotation of subinertial tides near the bottom, tidal effects are still present close to the bottom after the tidal flow found from the interior is removed. This may be the cause of the eddy like flow pattern in the plume.

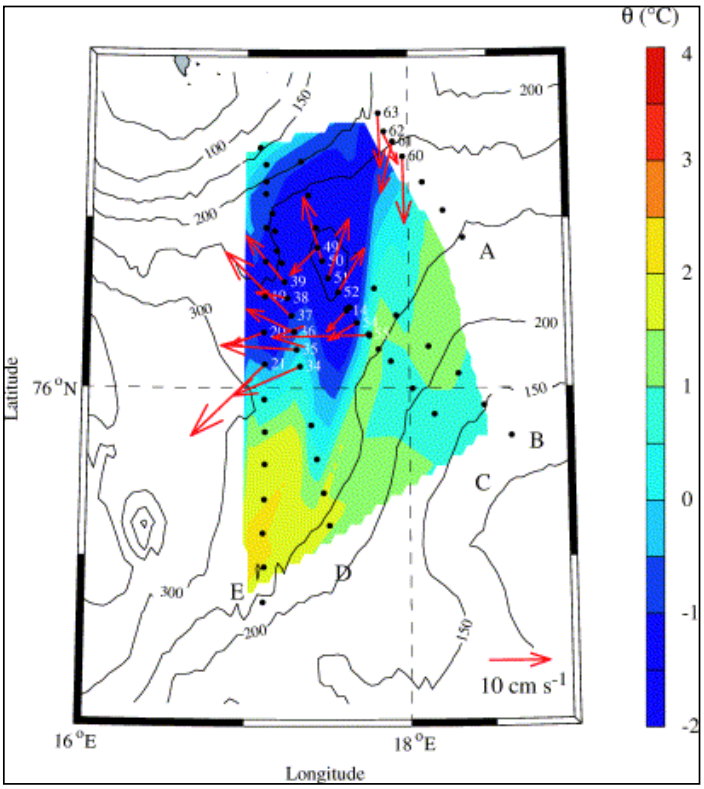

Fig. 12. Spatial distribution of isotherms at the bottom (colored) and the depth contours at 50 m intervals (black). The isotherms are drawn at 0.5°C intervals. The stations are shown by dots with station numbers indicated. The arrows show the plume velocity averaged over the plume height relative to the ambient water measured by the LADCP. Additional arrow in the lower right corner is the scale for the velocity.

5. Discussion

5.1. Bulk and local mixing

Based on 2-D experiments of gravity currents on sloping and horizontal surfaces covering a broad range of parameters, [Ellison and Turner (1959)] derived a dynamical model for the bulk properties of the flow for non-rotating systems. They presented a theory in which it is assumed that the velocity of inflow entrained into the turbulent gravity current must be proportional to the velocity scale of the current; the constant of proportionality is called the entrainment coefficient, E. They predicted and experimentally verified that an inclined gravity current will rapidly attain an equilibrium state in which the overall Richardson number, Ri_o, does not vary with distance downstream, and the gravitational force on the layer is just balanced by the drag due to entrainment together with the friction on the floor. Ri_o is a parameter specifying the *overall* state of a vertical cross-section of the gravity current, and is defined as

$$Ri_o = \frac{g' h}{\delta U^2}, \tag{2}$$

where δU is the velocity difference between the gravity current and the ambient water, h is the thickness of the gravity current and g' is the reduced acceleration of gravity. Some authors prefer to incorporate the bottom layer velocity rather than δU; however, when the ambient flow is weak the differences are minor. The inverse square root of Ri_o is the internal Froude number, Fr. The experiments of Ellison and Turner show that the entrainment coefficient, E, falls off rapidly as Ri_o increases and is weak when Ri_o is greater than about 0.8. Further experimental evidence compiled by [Turner (1973)] on a Ri_o–E space shows that E drops from 10^{-2} near Ri_o=1 to less than 10^{-4} at Ri_o=10, a trend also supported by streamtube model applications to Denmark Strait and Mediterranean overflows ([Smith (1975)]). For sufficiently high Fr interfacial instabilities such as roll waves, or intermittent surges, may develop ([Armi (1977)]; [Fer et al (2002)]).

We have evaluated Ri_o between layer 2 and the ambient waters using the relative speed of layer 2 with respect to the ambient water (see Fig. 10d for section averaged values). When Ri_o is derived over the plume height, it increases by a factor of two, on the average. In both cases Ri_o suggests stability and reduced entrainment within the observed part of the plume. Here, Ri_o and the associated Froude numbers are comparable to those reported for most parts of the Mediterranean overflow ([Baringer and Price (1997)]) where Fr varied within $0.3<Fr<0.8$ (equivalently, $11>Ri_o>1.6$) except for a couple of localized mixing regions with $Fr>1$ at the early part of the overflow. Furthermore, estimates of the mean Ri_o using the velocity profiles having the best-defined two-layered structure near the sloping sides are within the range of 2–4. The width of layer 2 increases from about 22 to 38 km (Table 3) along its path of 37 km

leading to an entrainment rate of about 5×10^{-4}, when the layer thickness (35 m) and speed (0.15 m s^{-1}) are assumed constant. A comparison of layer 2 between sections A and E suggests that the thickness is almost constant with a mean value of 21 m (Table 3). Estimates of the entrainment rate and Ri_o compare well with those obtained from moorings in the same region in the past ([Schauer and Fahrbach (1999)]), as well as those obtained from laboratory experiments of turbulent gravity currents flowing down a slope compiled by [Turner (1973)], Fig. 6.8).

In a shear flow the gradient Richardson number, the non-dimensional ratio of the density gradient over the velocity gradient, is expressed by

$$Ri = \frac{(g/\rho_0)\partial\rho/\partial z}{|\partial \mathbf{u}/\partial z|^2}, \quad (3)$$

where **u** is the horizontal velocity vector, ρ_0 is a reference density, and g is the gravitational acceleration. A sufficient condition for stability is obtained when $Ri \geq 0.25$ (see e.g., [Turner (1973)]) and energy may propagate in the form of internal gravity waves. At smaller *Ri*, Kelvin–Helmholtz instabilities may grow and overturning occurs, producing patches of turbulence and vertical mixing. We have estimated *Ri* using the density profiles derived from the CTD measurements and the horizontal velocity from the LADCP profiles. The profiles of *Ri* estimated over 1-, 3-, and 5-m intervals at the stations where the core of the overflow is observed are shown in Fig. 13 within 100 m above bottom. The estimates of *Ri* are sensitive to the length scale over which the vertical gradients are computed; however, all profiles show portions where $Ri<0.25$ in the proximity of the plume–ambient water interface, marked by arrows in Fig. 13. Therefore we note that in a regime characterized by weak entrainment in an overall state, we might expect localized unstable features with *Ri* below critical value.

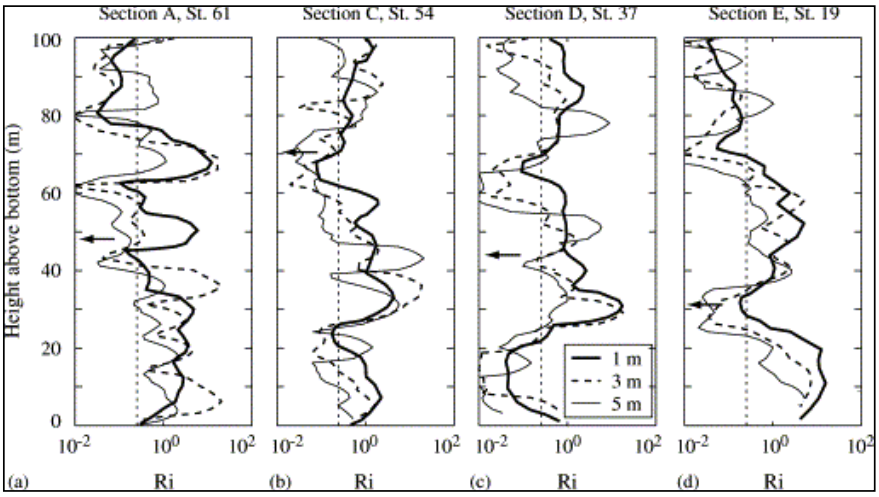

Fig. 13. Profiles of the gradient Richardson number, *Ri*, with respect to height above bottom, calculated over 1 (thick line), 3 (dashed line), and 5-m (thin line) vertical separations at the core of the plume at sections (a) A, (b) C, (c) D, and (d) E. The arrows mark the height of the plume. The dashed, vertical line is the critical *Ri* equal to 0.25. The legend in (c) is identical for all panels.

The mean temperature–salinity characteristics of the plume (Table 3) suggest that en route from sections A to E layer 1 almost preserves its properties, notably getting slightly denser. Assuming that the overflow has θ=–1.8°C and S=35.1 near the sill, it has to entrain 4 parts of ambient water per 7 parts of source water during its path to section A to yield the characteristics of layer 1. Here, i.e. at the early parts of the overflow, the ambient water is the ESW with approximately θ=–0.7°C and S=34.8. On the other hand, Layer 1 of section A will have to mix with the AW of approximately θ=3°C at a rate of 3:1 and 2:1 to reach the temperatures derived for layer 2 at sections A and E, respectively. However, it should be noted that layer 2 is associated with salinities lower than both the AW and layer 1. This suggests that there may be a supply of saline water into layer 1 as well as less saline water into layer 2, probably from the shelf south of Svalbard (see e.g. tongue of θ<1°C and S>34.8 bottom water at station 45 in Fig. 8). The frontal mixing associated with the Polar Front may lead to cabbeling when the densities of the AW and the Arctic water are equal. The product water will be colder, fresher, and slightly denser than the AW, and may explain the low salinity of layer 2. The maximum salinity and the minimum temperature recorded at the core of the plume (Table 4) indicate increase in salinity and decrease in temperature with downslope distance, in contrast with the entrainment arguments. The densest, coldest and most-saline downstream layer 1 is most likely remnants from earlier overflows and the gradients resulting from time-varying source water conditions. The depth of the water column where the core of the overflow is observed suggests a downflow from a depth of 263 to 302 m from sections A to D. At section E, however, station 19 comprises the densest water even though it lies over 275-m isobaths (Table 4, see also Fig. 9). It is reasonable to consider that the plume flowed down to 318-m depth, station 20, at section E, whereas the dense water recorded at station 19 is remnants of an earlier episode of denser overflow, which was trapped by the irregular topography (note the depression between stations 18 and 20 in Fig. 9).

Table 4. Properties of the plume at its core

Section/station	A/61	C/54	D/37	E/19	E/20
Height (m)	18/30	30/40	28/16	9/22	7/6
Depth (m)	263	304	302	275	318
θ (°C)	−1.14	−1.02	−1.54	−1.63	−0.64
S	34.91	34.93	34.97	34.99	34.98
σ_θ	28.08	28.08	28.14	28.16	28.11
θ_{min} (°C)	−1.63	−1.73	−1.77	−1.79	−1.35
S_{max}	35.02	35.04	35.08	35.09	35.04

Station 20 of section E is also included. Plume height is given as thickness of layer 1/layer 2, separately. Depth is the total depth of the water column where the core is observed. Temperature, θ, salinity, S, and $\sigma\theta$ are averaged over the height of the plume. θ_{min} and S_{max} are the minimum temperature and maximum salinity, respectively, recorded at each station.

5.2. Spreading of the plume

The increase in width of both layers 1 and 2 from sections A to E can also be driven by Ekman veering. Ekman veering within an overflow is expected to produce secondary circulation where lighter water within the interface (layer 2, here) would deviate in an anti-cyclonic sense whereas dense bottom water (layer 1, here) would deviate in a cyclonic sense from the direction of the flow. Ekman veering has been reported for Faroe Bank Channel ([Johnson and Sanford (1992)]) and the Mediterranean ([Baringer and Price (1997)]) overflows. Fig. 14 shows the layer averaged velocity derived for both layers of sections A and E for the stations where both layers are present. The deviation in average velocities from layer 2 to layer 1 is in the Ekman sense. An ensemble average of the angle between the mean velocity in layer 2 and that in layer 1 yields a veering of 4±2.5° (±standard error) counterclockwise with depth, relative to layer 2. This corresponds to a spreading of 7±4 km in 100 km downstream distance. Our observations show a spreading of around 6 and 16 km for layers 1 and 2, respectively, over the plume's approximate path of 105 km (Table 3, also note that the width of layer 2 indicates the width of the plume, since it overlays layer 1). The widening of layer 1 is comparable to the Ekman spreading whereas that of the plume in total is considerably larger.

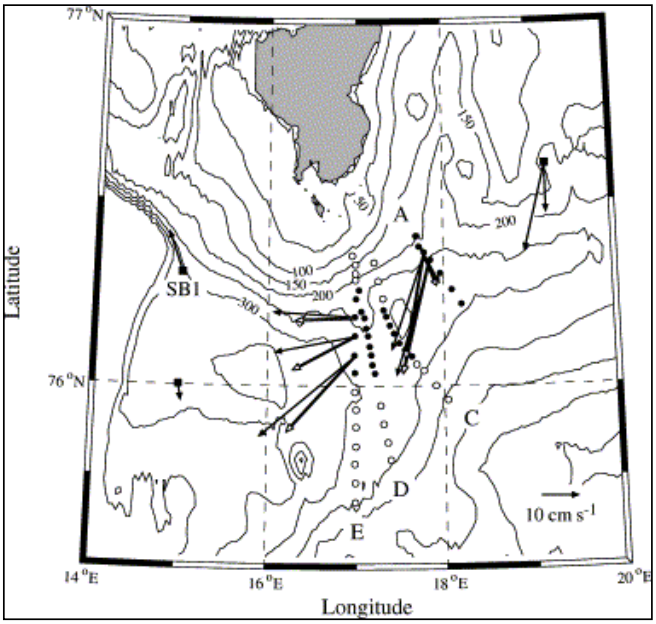

Fig. 14. Layer averaged velocity derived for layer 1 (open arrows) and layer 2 (solid arrows) of the selected stations. Circles and dots indicate the CTD and CTD–LADCP stations, respectively. The arrows drawn at stations marked by filled squares show the yearly mean velocities of the flow near the bottom observed during 1993–1994 (the larger vector at the upper right station is observed during 1991–1992) ([Schauer and Fahrbach (1999)]). The location of the mooring SB1, the data of which are used to derive the tidal ellipses shown in Fig. 4, is also indicated.

5.3. Volume transport

In order to estimate the net volume transport of the plume through sections A and E we converted the velocity measured by the LADCP into along and across-section components. Standard error of the velocity measured by the LADCP varies within 1–3 cm s^{-1} for the constant-depth sampling portions (see Section 3). The transport calculated for layer 1 is 0.026±0.005 Sv out of section A, increasing to 0.031 ±0.005 Sv out of section E. Corresponding values for layer 2 are 0.034±0.01 and 0.093±0.01 for sections A and E, respectively. The total transport of plume water through section E can be roughly estimated as

0.12±0.015 Sv, i.e. sum of both layers. Here, the uncertainties are derived from the standard error of the velocity. Errors in representative volume calculations and tidal aliasing may also lead to higher uncertainties, and, as mentioned earlier, LADCP velocity field is a snapshot and may not be representative of the long-term mean. However, this is an order of magnitude estimate which agrees well with earlier estimates of 0.13 Sv through 5 months of observations when the overflow occurred or 0.05 Sv when averaged annually ([Schauer (1995)]) and 0.12 Sv and 0.11 Sv through numerical simulations of [Backhaus et al (1994)] and [Jungclaus et al (1995)], respectively. It can be shown that the weak entrainment, E~5×10^{-4}, can account for the doubling of the volume transport from sections A to E. The entrainment velocity, w_e, for a typical plume speed of u=0.15 m s^{-1} is $w_e=Eu=7.5\times10^{-5}$ m s^{-1}. The plume will entrain the overlying water over a surface area, S, of 37 km (alongstream path between two sections) ×22 km (width of the plume at section A), neglecting the increase in width with downstream distance. The associated volume transport will then be Sw_e equal to 0.06 Sv.

The cyclonic circulation of the AW may lead to a downwelling of the relatively dense waters adjacent to the sloping side. Classical Ekman theory shows that a boundary layer of thickness $\delta_E=\kappa u_*/f$ develops for turbulent flows where κ=0.4 is the von-Karman's constant and u_*, the friction velocity, can be estimated as ~3% of the ambient, geostrophic velocity, V ([Turner (1986)]). The transverse transport associated with this downwelling is $V\delta_E/2$ ([Pedlosky (1979)]). For V=0.1 m s^{-1} (see Fig. 11a and b) this leads to an Ekman boundary layer thickness of approximately 10 m using f=1.4×10^{-4} s^{-1}. The transverse transport is then 0.5 m^2 s^{-1} per unit width of the slope, which integrated over about 20 km, the approximate distance between station 63 and 15, i.e. onshore-most stations of sections A and E, yields 0.01 Sv. Fig. 7 and Fig. 8 suggest that the water nested on the onshore sloping side has the approximate density of layer 2, and while draining may find an equivalent depth in layer 2, thus leading to an increase in volume. This is about 17% of the transport associated with the plume at section A and may explain 17% of the increase of the volume transport through section E which has doubled from section A.

5.4. Rate of descent of the overflow

Recently, [Killworth (2001)] has suggested and subsequently applied a simple model to predict the path taken by dense turbulent overflows, assuming a quadratic turbulent bottom drag and an approximate local equilibrium which is approximately equivalent to a constant Ri_o. The path is determined by a constant rate of descent, independent of the detailed thermodynamics, entrainment or detrainment. The flow deviates from the eastward direction at an angle ϕ,

$$\phi = \lambda \pm \cos^{-1}\left(\frac{1}{C_i^2|\nabla D|}\right), \tag{4}$$

where D is the topography depth and λ is the angle ∇D makes with the east. Here C_i is a constant equal to 20 and $1/C_i^2$=1/400 provides for an upper limit for the rate of vertical descent of the overflow along the slope (for details and discussion on the effects of entrainment and detrainment see [Killworth (2001)]). Given a start location and a chosen sign depending on the hemisphere, i.e. on the sign of the Coriolis parameter, the path of the overflow can be predicted. The overflow is allowed to descend along the maximum downward slope when the local slope is smaller than the descent rate.

The path of the Storfjorden overflow predicted by Eq. (4) is shown in Fig. 15 for both the smoothed and the original bathymetry. The starting point is chosen about 8 km downstream of the sill, approximately twice the typical Rossby radius, allowing for the rotational effects to be established. Killworth in his calculations of the major overflow paths (Mediterranean, Denmark Strait, Faroe Bank and the Weddell Sea overflows) has used slightly smoothed topography. Probably because of the irregular topography of Storfjorden, the path predicted using the real bathymetry captures the stations where we observed the core of the plume (marked by circles and corresponding station numbers in Fig. 15).

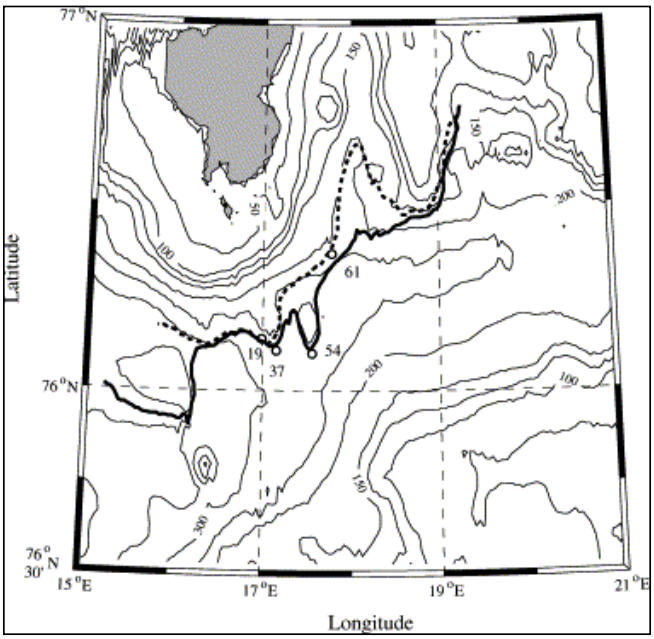

Fig. 15. Predicted path of the Storfjorden overflow using [Killworth (2001)] model for a descent rate of 1/400 calculated over real bathymetry (solid line) and smoothed bathymetry (dashed line). The topography contour interval is 50 m and the 125 m isobath is included to identify the location of the sill. The circles and the corresponding numbers are the stations where the core of the Storfjorden plume was observed during the cruise.

6. Concluding remarks

Our measurements suggest that the downstream development of the Storfjorden overflow cannot be explained by means of simple entrainment and mixing between *two* different water masses. We have identified the overflow by two layers underlying the ambient Atlantic Water. The denser lower layer appears to be the remnants from earlier overflows and it almost maintains its temperature–salinity characteristics while spreading about 6 km over its path, comparable to the Ekman veering. The mixing layer above is relatively thicker and increases both in width and the associated volume transport over the plume's path. The light transmissivity is relatively low within the overflow probably because of enhanced suspended sediment concentration as a result of bottom-intensified currents. The overall properties of the observed part of the plume suggest dynamical stability with weak entrainment; however, locally, portions where Kelvin–Helmholtz instabilities may grow are identified in the vicinity of the plume–ambient water interface.

The new multilayer description of the plume, the associated shear-induced mixing process and the documented effect of bottom friction has shed some new light on downstream development of the overflow. However, this is a complex phenomenon which is not yet fully understood. Additional mechanisms including frontal mixing along the Polar Front, Ekman drainage under an alongslope current, wind-driven downwelling, and particularly the draining due to the winter cooling of shallow and wide shelf regions with consequent contributions to the overflow merit further investigations. Furthermore, the bathymetry of the site is not well resolved and the possibility of submarine canyons cutting across the slope may alter the mixing dynamics significantly. Therefore, needs in future studies include improved bathymetry and detailed studies of the shelf.

Acknowledgements

This work was funded by the Norwegian Research Council, through grants 147493/432 for IF and 138525/410 for RS. The fieldwork was supported through the NOClim (Norwegian Ocean Climate) project funded by the Norwegian Research Council, grant 139815/720. U. Schauer is acknowledged for kindly providing the SB1 data. IF thanks S.A. Thorpe for reading an earlier version of the manuscript. We thank the captain and crew of the R.V. *Lance*, V. Tverberg and H. Goodwin for their help during the cruise, and F. Nilsen who provided the LADCP. Comments from two anonymous reviewers improved an earlier version of this paper. This is publication number A0025 of the Bjerknes Centre for Climate Research.

References

Anderson et al (1988). L.G. Anderson, E.P. Jones, R. Lindegren, B. Rudels and P.I. Sehlstedt, Nutrient

regeneration in cold, high salinity bottom water of the Arctic shelves. *Continental Shelf Research* **8** (1988), pp. 1345–1355.

Armi (1977). L. Armi, The dynamics of the bottom boundary layer of the deep ocean. In: C.J.J. Nihoul, Editor, *Bottom Turbulence, 8th Int. Liège colloq. on Ocean hydrodynamics*, Elsevier, Amsterdam (1977), pp. 153–164.

Backhaus et al (1994). Backhaus, J.O., Fohrmann, H., Harms, I.H., Jungclaus, J.H., Rubino, A., 1994. Convective water mass and ice formation in arctic shelf seas—numerical process studies. Proceedings of the ACSYS Conference on the Dynamics of the Arctic Climate System, World Climate Research Program, Gothenburg, Sweden, pp. 83–95.

Baines and Condie (1998). P.G. Baines and S. Condie, Observations and modelling of Antarctic downslope flows: a review. In: S. Jacobs and R. Weiss, Editors, *Ocean, Ice and Atmosphere: Interactions at the Antarctic Continental Margin. Antarctic Research Series* **Vol. 75**, American Geophysical Union, Washington, DC (1998), pp. 29–49.

Baringer and Price (1997). M.O. Baringer and J.F. Price, Mixing and spreading of the Mediterranean outflow. *Journal of Physical Oceanography* **27** (1997), pp. 1654–1677.

Ellison and Turner (1959). T.H. Ellison and J.S. Turner, Turbulent entrainment in stratified flows. *Journal of Fluid Mechanics* **6** (1959), pp. 423–448.

Fer et al (2002). I. Fer, U. Lemmin and S.A. Thorpe, Winter cascading of cold water in Lake Geneva. *Journal of Geophysical Research* **107** C6 (2002), p. 3060 doi:10.1029/2001JC000828 .

Foldvik et al (2001). A. Foldvik, T. Gammelsrød, E. Nygaard and S. Østerhus, Current measurements near Ronne Ice Shelf: implications for circulation and melting. *Journal of Geophysical Research* **106** (2001), pp. 4463–4477.

Furevik and Foldvik (1996). T. Furevik and A. Foldvik, Stability at M_2 critical latitude in the Barents Sea. *Journal of Geophysical Research* **101** (1996), pp. 8823–8837.

Gjevik et al (1994). B. Gjevik, E. Nøst and T. Straume, Model simulations of the tides in the Barents Sea. *Journal of Geophysical Research* **99** (1994), pp. 3337–3350.

Gordon et al (2001). A.L. Gordon, M. Visbeck and B. Huber, Export of Weddell Sea deep and bottom water. *Journal of Geophysical Research* **106** (2001), pp. 9005–9017.

Griffiths (1986). R.W. Griffiths, Gravity currents in rotating systems. *Annual Review of Fluid Mechanics* **18** (1986), pp. 59–89.

Haarpaintner et al (2001a). J. Haarpaintner, J.-C. Gascard and P.M. Haugan, Ice production and brine formation in Storfjorden, Svalbard. *Journal of Geophysical Research* **106** (2001), pp. 14001–14013.

Haarpaintner et al (2001b). J. Haarpaintner, P.M. Haugan and J.-C. Gascard, Interannual variability of the Storfjord ice cover and ice production observed by ERS-2 SAR. *Annals of Glaciology* **33** (2001), pp. 430–436.

Johnson and Sanford (1992). G.C. Johnson and T.B. Sanford, Secondary circulation in the Faroe Bank Channel outflow. *Journal of Physical Oceanography* **22** (1992), pp. 927–933.

Jungclaus et al (1995). J.H. Jungclaus, J.O. Backhaus and H. Fohrmann, Outflow of dense water from the Storfjord in Svalbard: a numerical model study. *Journal of Geophysical Research* **100** (1995), pp. 24719–24728.

Killworth (1983). P.D. Killworth, Deep convection in the world ocean. *Reviews of Geophysics* **21** (1983), pp. 1–26.

Killworth (2001). P.D. Killworth, On the rate of descent of overflows. *Journal of Geophysical Research* **106** (2001), pp. 22267–22275.

Kowalik (1994). Z. Kowalik, Modeling of topographically amplified diurnal tides in the Nordic Seas. *Journal of Physical Oceanography* **24** (1994), pp. 1717–1731.

Kowalik and Proshutinsky (1993). Z. Kowalik and A.Y. Proshutinsky, Diurnal tides in the Arctic Ocean. *Journal of Geophysical Research* **98** (1993), pp. 16449–16468.

Loeng (1991). H. Loeng, Features of the physical oceanographic conditions of the Barents Sea. *Polar*

Research **10** (1991), pp. 5–18.

Midttun (1985). L. Midttun, Formation of dense bottom water in the Barents Sea. *Deep-Sea Research Part A* **32** (1985), pp. 1233–1241.

Pawlowicz et al (2002). R. Pawlowicz, B. Beardsley and S. Lenz, Classical tidal harmonic analysis including error estimates in MATLAB using T-TIDE. *Computers and Geosciences* **284** (2002), pp. 929–937.

Pedlosky (1979). J. Pedlosky. *Geophysical Fluid Dynamics*, Springer, New York (1979).

Price and Baringer (1994). J.F. Price and M.O. Baringer, Outflows and deep water production by marginal seas. *Progress in Oceanography* **33** (1994), pp. 161–200.

Quadfasel et al (1988). D. Quadfasel, B. Rudels and K. Kurz, Outflow of dense water from a Svalbard fjord into the Fram Strait. *Deep-Sea Research* **35** (1988), pp. 1143–1150.

Rudels (1986). B. Rudels, The θ–S relations in the northern seas: implications for the deep circulation. *Polar Research* **4** (1986), pp. 133–159.

Rudels and Quadfasel (1991). B. Rudels and D. Quadfasel, Convection and deep water formation in the Arctic Ocean–Greenland Sea system. *Journal of Marine Systems* **2** (1991), pp. 435–450.

Schauer (1995). U. Schauer, The release of brine-enriched shelf water from Storfjord into the Norwegian Sea. *Journal of Geophysical Research* **100** (1995), pp. 16015–16028.

Schauer and Fahrbach (1999). U. Schauer and E. Fahrbach, A dense bottom water plume in the western Barents Sea: downstream modification and interannual variability. *Deep-Sea Research I* **46** (1999), pp. 2095–2108.

Skogseth et al (2003). Skogseth, R., Haugan, P.M., Jakobsson, M., 2003. Water mass transformations in Storfjorden. Continental Shelf Research, submitted.

Smethie et al (1986). W.M. Smethie, H.G. Ostlund and H.H. Loosli, Ventilation of the deep Greenland and Norwegian Seas: evidence from Krypton-85, Tritium, Carbon-14, and Argon-39. *Deep-Sea Research Part A* **33** (1986), pp. 675–703.

Smith (1975). P.C. Smith, A streamtube model for bottom boundary currents in the ocean. *Deep Sea Research* **22** (1975), pp. 853–873.

Turner (1973). J.S. Turner. *Buoyancy Effects in Fluids*, Cambridge University Press, New York (1973).

Turner (1986). G.L. Weatherly, A numerical study of time-dependent turbulent Ekman layers over horizontal and sloping bottoms. *Journal of Physical Oceanography* **5** (1975), pp. 288–299.